Impact of Hybrid Electromagnetic Surface Modes on the Formation of Low Spatial Frequency LIPSS: A Universal Approach

George Perrakis,* Odysseas Tsilipakos, George D. Tsibidis, and Emmanuel Stratakis*

In this article, the impact of the excited electromagnetic surface modes in a comprehensive investigation of the formation of laser-induced periodic surface structures (LIPSS) is analyzed. It is demonstrated that the electromagnetic origin of low spatial-frequency LIPSS (LSFL) is the frequency detuning between propagating and localized modes due to their coupling/hybridization. The influence of the pattern profile, inhomogeneity, and material type on the coupling strength, electric-field spatial distribution, and associated near-field scattering are highlighted. Exploiting the potential of the approach, evidence of a universal manifestation of LSFLs is provided irrespective of the material and the authors are able to predict and validate the experimentally-proven lower limit of LSFL periodicity (i.e., $\lambda_L/2$, where λ_L stands for the laser wavelength). Furthermore, the analysis of the electromagnetic modes predicts that the periodicity of LSFL is practically unaffected by the laser fluence, while a suppression of LSFL at high excitation levels or large number of pulses is also predicted. It is also shown that plasmonic-active materials are not necessary for LSFL formation perpendicular to polarization. Toward these directions, an important generic metric, namely the resonance quality factor, is additionally inserted. The approach can, thus, serve as a guide for controlling laser-induced surface topography.

1. Introduction

The interaction of light with corrugated surfaces and gratings leads to a plethora of optical effects tunable by the geometric design and attracts a broad scientific interest. Notably, the realization of laser-induced periodic surface structures (LIPSS) with ultrashort pulsed lasers represents a promising candidate for the surface nanostructuring of a broad range of materials (i.e., metals, semiconductors, dielectrics, and polymers) through a low-cost, robust, and scalable approach. LIPSS periodicity can be controlled via the modulation of the laser parameters while the fabricated topographies can be exploited for impressive functionalities in a broad range of applications[1] such as broadband, omnidirectional antireflection,[2,3] perfect absorption,[4] and efficient beam polarization control,[5] enhanced thermal response such as cooling,[3] as well as water repellent and antimicrobial properties.[6,7]

Despite their successful realization, the elucidation of the underlying physical processes leading to LIPSS formation is a long-debated topic in optics and condensed matter physics. This is because different multiscale physical mechanisms are involved, such as energy absorption, carrier excitation and thermalization, and various thermal and structural events, making it an intricate problem.[8] A widely accepted electromagnetic theory was proposed by Sipe et al. in the 1980s,[9,10] where surface nano-roughness acts as a broadband random grating providing sufficient momentum to collectively excite surface-scattered waves. The interference of the incident laser pulse and induced surface-scattered waves results in a periodic optical intensity variation along the surface which leads to a modulation of the surface via mass transfer (melting due to Joule heating) or removal (ablation) or simply a variation of the material properties via the thermo-optic effect.[11] Therefore, the long-range order and orientation of LIPSS are dictated by the excitation strength, propagation phase, and direction of surface-scattered waves, whose periodicity determines the structural periodicity.[9,10,12]

Nevertheless, despite its remarkable insight, Sipe's theory cannot model light-matter interaction for any arbitrary surface geometry.[13–15] Furthermore, due to the self-organization

G. Perrakis, G. D. Tsibidis, E. Stratakis
Institute of Electronic Structure and Laser (IESL)
Foundation for Research and Technology-Hellas (FORTH)
Heraklion, Crete 70013, Greece
E-mail: gperrakis@iesl.forth.gr; stratak@iesl.forth.gr
O. Tsilipakos
Theoretical and Physical Chemistry Institute
National Hellenic Research Foundation
Athens 11635, Greece
E. Stratakis
Department of Physics
University of Crete
Heraklion 71003, Greece

of matter into more complex structures through consecutive irradiation,[15–18] Sipe's theory often fails to describe topography-related interpulse feedback effects.[12,13,19,20] As a result, along with the debate regarding the nature of the resulting surface waves, the origin of low spatial-frequency LIPSS (LSFL) with a periodicity that varies with the number of applied laser pulses (N) between $\lambda_L/2$ and λ_L (λ_L is the illuminating laser wavelength) has remained largely unexplored, despite the several experimental observations.[8,13,15,21] Furthermore, while most research studies were predominantly focused on the interpretation of the pronounced decrease of the ripple periodicity at increasing number of pulses, the experimentally-observed insignificant influence of the laser fluence on the periodicity is still not fully discussed.[21–23]

A plethora of theoretical studies have predominantly focused on numerical approaches adopting primarily the finite-difference time-domain method to model light-matter interaction for any geometry by solving Maxwell's equations.[8,13,15,24] While significant advances have been accomplished toward determining the origin of LIPSS, the relevant electromagnetic mechanisms as well as the interplay of the excited surface waves are yet to be fully explored.[12,25] This is due to the complexity and plethora of the underlying electromagnetic effects generated from interpulse material removal or mass transfer; thus, it appears that the light-driven surface topography gradually evolves upon irradiation by multiple femtosecond laser pulses, and the nature, properties, and effect of the resulting surface modes highly depends on the surface relief and material. Theoretical and experimental studies aimed to analyze interpulse phenomena have revealed the transition from a rough surface to a pronounced sinusoidal-type rippled (grating) profile (both on metals and semiconductors) as well as the decrease of the ripple periodicity with N.[21,26] However, the theoretical examinations conducted to elucidate the electromagnetic mechanisms related to LIPSS formation and ripple's periodicity tuning with N have mainly considered shallow topographies, that is, random distribution of nanoholes or nanobumps (mainly metallic), or dipole approximations.[13,15,20,24] Consequently, there is still a need for a comprehensive EM analysis that thoroughly examines the impact of ripple depth, inhomogeneity (or asymmetry, that is, deviation from a sinusoidal ripple), and material on LIPSS formation and periodicity.

To address the above challenges, in this work, we present a detailed analysis of the excited electromagnetic modes that act as precursors for the induced LIPSS. We consider ripples with different periodicity, depth, and shape for a broad range of frequencies and incident angles, to provide numerical insight into the origin, properties, and interplay of the produced surface modes depending on the induced topography and material and analyze their impact on the LIPSS features. In particular, we consider a realistic ripple geometry by assuming ripples of a periodic surface-relief profile given by a Fourier series of higher-order harmonic components of the corrugation and varying amplitude, to emulate surface-relief modification due to melting and/or ablation leading to laser-induced inhomogeneities and high modulation depths.[15,17,18,27] While the proposed methodology is performed on stainless steel and silicon, the overall strategy is aimed to set the basis for a novel interpretation of LIPSS formation irrespective of the material type.

2. Results and Discussion

2.1. Electromagnetic Feedback Mechanisms Enhancing the Q-Factor and Generating LSFL Formation

In order to elucidate the process of LSFL formation and the tuning of their periodicity we need to study the physical mechanisms that mediate the generation of LIPSS with periodicities in the order of the laser wavelength and orientation related to the laser electric field polarization.[21,28] Following the principles of standard electromagnetic theory,[9,10] the manifestation of a single periodicity that dominates the surface topography is the outcome of a "positive electromagnetic feedback" process from pulse to pulse, resulting in the amplification of patterns with this particular periodicity.[29] Thus, the generation of LSFLs requires an increase of the absorbed energy on the surface by coupling light to propagating surface modes (such as SPPs, for example).[30] In addition, it is desirable for the guided mode to have a long propagation length (low energy decay). In other words, viewed as a guided mode resonance, the quality (Q)-factor (defined as $Q = \lambda_{res}/\Delta\lambda$, where $\Delta\lambda$ is the FWHM of the absorption peak and λ_{res} the resonance wavelength)[31] should be high enough to increase the number of photons along the metal surface and their interaction time with the material. Furthermore, enhancement of the Q-factor should be a positive electromagnetic (EM) feedback process from pulse to pulse; this is expected to allow the laser power to be efficiently transferred to the EM mode resulting in the amplification of patterns with a specific periodicity.

On metal surfaces, surface plasmon polaritons (SPPs) lead to LSFL formation with periods of $\approx\lambda_{SPP}$.[8,32] They are excited even in the case of nano-roughness (irregular and very shallow topography), which provides sufficient momentum matching of the photon and the SPP.[9,10,32] In multipulse scenarios, the evolution of the surface relief can result in an asymmetric, inhomogeneous ripple profile (corresponds to higher Fourier components); this influences the local energy deposition from pulse to pulse and hence affects LSFL formation and periodicity. For example, as the surface relief evolves, localized resonances[33] may be supported, which are tightly confined within the ripple trough and do not significantly overlap with the propagating SPP field. Intermediate cases where the localized modes couple/hybridize with SPP-type modes propagating on the surface of the ripple, thus dictating the frequency and linewidth of efficient absorption are common in plasmonic systems such as metallic gratings or nanoparticle arrays.[33] Viewed as guided mode resonances, λ_{res} and Q are modified,[31] thus affecting LSFL formation and periodicity. The enhanced radiative coupling can be mediated by: i) the diffraction/scattered orders in the plane of the array (i.e., Rayleigh anomalies, RAs) and ii) planar waveguided modes, (e.g., SPPs on metal surfaces). The hybridization of localized surface plasmon resonances (LSPRs) with RAs results in hybrid or coupled surface modes, widely known as surface lattice resonances (SLRs).[34]

2.2. Optical Evaluation of Hybrid Surface Mode on Metal LSFL

In order to gain physical insight into laser-induced surface patterning, we examine geometries that correspond to typical laser processing configurations upon irradiation of a bulk material
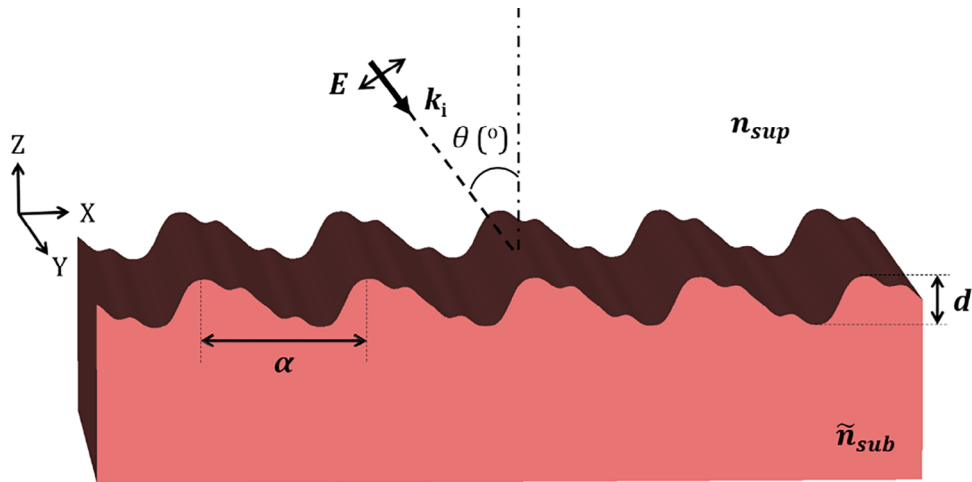
ADVANCED
SCIENCE NEWS
www.advancedsciencenews.com

LASER
& PHOTONICS
REVIEWS

www.lpr-journal.org

Figure 1. A 2D simulation scheme with arbitrary incident angle θ and transverse-magnetic (TM) polarization, that is, E-field inside the xz–plane of incidence. LIPSS is modeled as a sinusoidal surface-relief with varying lattice constant α, depth d, and higher-order harmonic components of the corrugation m, according to Equation (1). It is noted that the dark area should not be confused with that being another material. It, simply, represents the shade of the surface of the irradiated region.

(**Figure 1**). However, without loss of generality, the conclusions extracted on the nature and properties of the hybrid modes and their impact on LIPSS topography may also be used as a guide for different configurations (e.g., thin films). For instance, the radiative coupling between the individual LSPRs may emerge from a guided mode of a slab waveguide.[34] The nature of the excited surface modes on metallic LSFLs (stainless steel) are, first, identified based on their spatial field distribution while the conditions for LSFL formation and tuning of LSFL periodicity are also determined. To consider realistic complex ripple profiles induced by successive laser pulses, we assume a ripple with a surface-relief profile given by the Fourier series (see also Figure 1),

$$f(x) = C_1 \sin(k_g x + \varphi_1) + C_2 \sin(2k_g x + \varphi_2)$$
$$+ \cdots + C_m \sin(mk_g x + \varphi_m) \quad (1)$$

where C_m is the amplitude of the mth order harmonic component of the corrugation, φ_m is the relative phase, and k_g is the x-component of the reciprocal lattice vector given by $k_g = 2\pi/\alpha$, where a is the lattice constant. The substrate material is de-

scribed by the complex dispersive refractive index $\tilde{n}_{sub}$ (i.e., material data are provided in ref. [35] for stainless steel) and $n_{sup} = 1$ is the refractive index of the superstrate material, in this case air (Figure 1).

We, first, assume a ripple of constant depth $d = 2 \bullet C_1 = 100$ nm, varying lattice constant in the range $\alpha = 540$–840 nm (i.e., typical LSFL periodicities for a laser wavelength $\lambda_L = 800$ nm according to experimental and theoretical results[18,36,37]), and varying asymmetry (higher-order harmonic components of the corrugation) in the range $m = 1$–4. The above selections are based on typical dimensions of a well-defined ripple pattern following irradiation with several pulses for fluences near the ablation threshold.[18,36,37] We first analyze reflectivity spectra at normal incidence (see **Figure 2**) defined as $R = \sum_l R_l$ (index l runs through the propagating diffraction orders for each frequency point).[33] The simulations are performed under transverse-magnetic polarization (TM) so that the electric field is inside the XZ–plane of incidence. The excited surface mode propagates perpendicular to the ripples (i.e., along the X–axis—see Figure 1 and Supporting Information for a detailed modeling description). We identify reflection dips (they correspond to absorption peaks) that
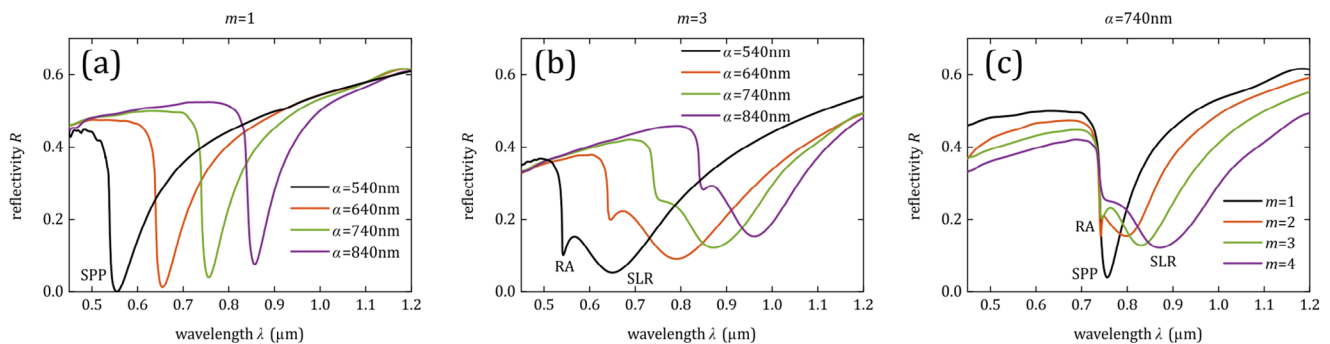

Figure 2. Reflectivity spectra at normal incidence for the structure depicted in Figure 1. a) Sinusoidal ripple ($m = 1$) and b) ripple with higher-order components ($m = 3$) with varying lattice constants of $\alpha = 540$, 640, 740, and 840 nm, respectively. c) The lattice constant is fixed at $\alpha = 740$ nm and the order of corrugation varies in the range $m = 1$–4.
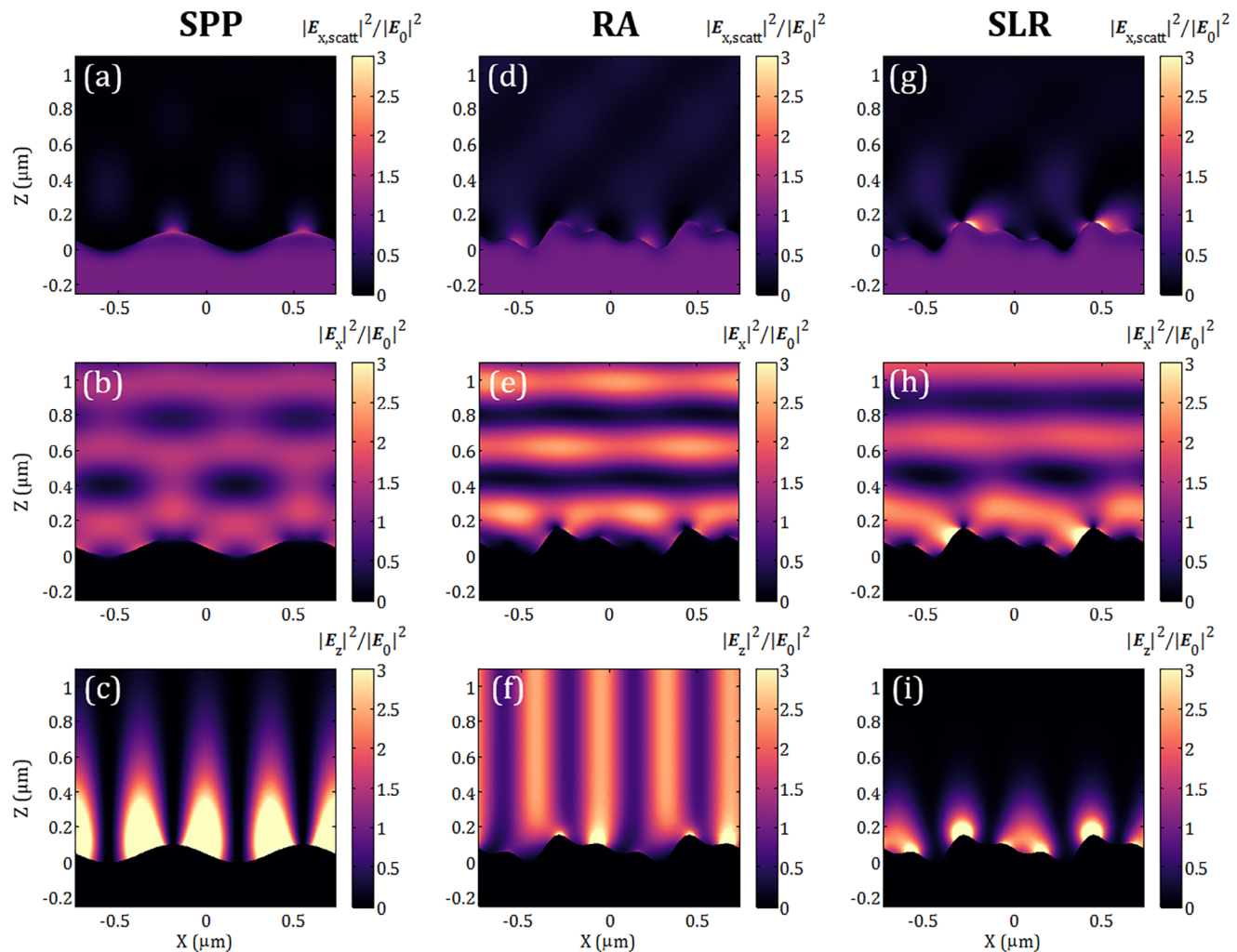
Figure 3. EM simulations of the spatial distribution of the electric field intensity normalized to the incident field intensity, $|E_0|,^2$ in the xz–plane of ripples with lattice constant $\alpha = 740$ nm. a–c) Distribution at $\lambda = 0.756$ μm corresponding to the SPP excitation on a ripple with $m = 1$ (see also green curve in Figure 2a). d–f) Distribution at $\lambda = 0.74$ μm corresponding to the RA excitation on a ripple with $m = 3$ (see also green curve in Figure 2b). The ± 1 diffraction orders have become propagating (predominantly real wavevector), corresponding to plane waves traveling along the $\pm x$–axis. f) The plane waves are not bound to the metal surface and no confinement along the z–axis is observed. g–i) Distribution at $\lambda = 0.871$ μm corresponding to the SLR excitation on a ripple with $m = 3$ (see also green curve in Figure 2c) that manifests at lower frequencies (longer wavelengths). The ± 1 diffraction orders are characterized by a predominantly imaginary wavevector (normal component), i) leading to exponential decay along the z (and x) axes. a,d,g) Normalized scattered electric field intensity of E_x, $|E_{x,\text{scatt}}|^2/|E_0|.^2$ b,e,h) Normalized electric field intensity of E_x, $|E_x|^2/|E_0|.^2$ c,f,i) Normalized electric field intensity of E_z, $|E_z|^2/|E_0|.^2$

are associated with the excitation of the surface modes and evaluate the nature of the excited surface modes based on their spatial field distribution (see **Figure 3**). More specifically, in Figure 3a,b, the scattered (after subtracting the incident) and total (scattered plus incident) electric field E_x component is plotted, respectively. In Figure 3c, the E_z component is depicted which is directly the scattered field since there is no component of the incident wave along Z. Note that the spatial field distribution in Figure 3 is calculated assuming LSFL ripples of $\alpha = 740$ nm, which corresponds to an initial LSFL surface relief arising after a small number of pulses (see experimental LSFL periodicity values in Figure S8a, Supporting Information, in purple color). Therefore, they are appropriate geometries to elucidate the evolution of the surface topography and periodicity reduction observed as the number of

ber of incident pulses increases further. Moreover, the simulations are performed in the frequency domain, and, therefore, the electric field results shown in Figure 3 correspond to temporally-averaged values.

For $m = 1$ and $\alpha = 540$–840 nm (Figure 2a), one pronounced minimum is observed in the reflectivity spectra. The dip wavelengths are found close to $\lambda = \alpha$. The surface corrugation results in the excitation of SPP surface waves on the metal-dielectric interface which manifests as a reflectivity minimum (or absorption peak, since transmission through the substrate is zero). We verify the nature of the excitation by observing the electric field distribution on the reflectivity dip. Results show that an SPP is guided along the metal surface (Figure 3c). For $m = 1$ and $d = 100$ nm, the shallow sinusoidal ripple can be considered to rep-

ADVANCED
SCIENCE NEWS

www.advancedsciencenews.com

www.lpr-journal.org

LASER
& PHOTONICS
REVIEWS

resent a relatively small perturbation of the planar interface. As a result, the wavelength of the reflectivity minimum (0.756 μm) lies close to 0.742 μm, which is calculated from the Bragg condition, $k_{SPP} = k_0 n_{sup} \sin\theta + 2\pi/\alpha$ (in our case $\theta = 0$), and the well-known dispersion relation for SPPs on planar metal-dielectric interfaces,

$$k_{SPP} = \frac{2\pi}{a} \Rightarrow k_0 \sqrt{\frac{\epsilon_{sup}\epsilon_m(\omega)}{\epsilon_{sup} + \epsilon_m(\omega)}} = \frac{2\pi}{\alpha} \qquad (2)$$

where $k_0 = \omega/c_0$ and c_0 are the wavenumber and the speed of light in vacuum, respectively, and $\epsilon_{sup} = n_{sup}2 = 1$ and ϵ_m (complex and dispersive) are the permittivity of the superstrate (i.e., air) and metal, respectively.

When m increases from $m = 1$ to $m = 3$ (Figure 2b), two pronounced minima are predicted. The short wavelength dip is due to the onset of the first diffraction order becoming propagating, which takes place when the respective reflected wavevector (normal component) becomes real. This is further corroborated in Figure 3f, which illustrates the (scattered) E_z component at $\lambda = 0.74$ μm for the case $\alpha = 740$ nm. The first diffraction order has just become propagating and leaves the structure at grazing angle (Figure 3), leading to the characteristic asymmetric resonance line shape (Rayleigh anomaly, RA) shown in Figure 2b. Specifically, Figure 3f indicates plane waves propagating at near grazing angle that are not bound to the metal surface, and no confinement along the Z–axis is observed. This happens when the lattice constant satisfies the Bragg scattering condition, that is,

$$\alpha\left[n_{sup} \pm \sin(\theta)\right] = l\lambda \qquad (3)$$

In contrast to the short wavelength dip observed in Figure 2b, the long wavelength dip corresponds to an SLR (of hybrid nature) and redshifts almost linearly with α. As seen by the field distributions in Figure 3g–i, ripples with higher-order Fourier components influence the local energy deposition. Figure 3g reveals localized excitations with a dipolar field pattern. Figure 3h indicates an enhanced radiative coupling compared to the case $m = 1$ (Figure 3b). This far-field coupling is diffractive in nature. More specifically, when the free-space wavelength approaches the lattice period, the ±1 diffraction orders are on the verge of becoming propagating in a direction parallel to the surface. Provided that the propagation length of this diffracted wave is long enough, it couples the individual localized resonances across the entire array.[38] These diffractively-coupled LSPRs manifest at somewhat lower frequencies (higher wavelengths) than the RA wavelengths (see Equation (3)).[38] The collective coupling of the dipolar LSPRs leads to a nonlocal excitation that coherently extends across the array (along the horizontal X–direction) confined on the metal surface (decays along the vertical Z–direction) (Figure 3i), which is termed an SLR.

In all cases (i.e., SPPs, RAs, and SLRs), enhanced fields on the surfaces are observed that can lead to energy absorption and the generation of LSFL structures. Note that the electric field results shown in Figure 3 correspond to temporally-averaged values, hence the distribution of the absolute value clearly indicates periodic optical intensity variation along the metal surface. Specifically, due to interference of the counter-propagating ±1 RAs and SPPs scattered by the surface toward both +X– and −X–

directions, standing waves are formed (see Figure S3, Supporting Information) that can modulate energy on average over the pulse duration, which leads to a modulation of the surface and the generation of LSFL structures. The associated higher absorption deposited beneath the metal surface in a periodic manner at λ_L is shown in Figure S4, Supporting Information. Specifically, the results in Figure S4, Supporting Information demonstrate a periodic energy deposition with symmetric or asymmetric profile (depending on ripples' asymmetry based on order m), in agreement with other studies showing the evolution of LIPSS surface relief as a function of the number of pulses.[15] However, results show (Figure 2c) that as m increases, the dispersive characteristics of SPPs and RAs differ from those of SLRs (resonance wavelength λ_{res} and linewidth). More specifically, simulation results illustrated in Figure 2c demonstrate a clear correlation between the SLR characteristics and the order of corrugation m. As m increases, λ_{res} lies further away from the RA, the SLR redshifts but also broadens indicating that the coupling strength between the localized resonances and RAs becomes stronger as m increases (see also differences in the enhanced neighboring field coupling in Figure 3b,h).[39] In the next sections, it will be shown that this shift of the SLR frequency with m plays a critical role in LSFL periodicity. As shown in Figure 2c, in the case of RAs and SPPs for a positive EM feedback process the laser wavelength should equal the ripple lattice constant, since the dip wavelengths are found close to $\lambda = \alpha$ (with narrow resonance bandwidth), in contrast, to SLRs.

Besides the λ_{res} shift, the increase of m naturally affects the resonance Q-factor (linewidth), and, thus LSFL formation. For instance, comparing Figure 3c with Figure 3i, a ripple curvature of higher order influences the near-field energy deposition (see enhanced near-field distribution at the higher order harmonic components of the corrugation). This enhanced near-field confinement naturally leads to higher ohmic losses, and hence, broader resonance linewidth and lower Q-factors (Figure 2c). Therefore, as m increases, the intensity of the near-field part of the SLR increases (or the Q-factor decreases), affecting, eventually, LSFL formation.

2.3. Impact of Order of Corrugation and Depth on Reflectivity

As a critical step to determine the conditions for controlling LSFL formation and periodicity with the number of pulses, N, we evaluate how the properties of the surface topography impact the resonance wavelength and Q-factor. Besides the initial irregular but shallow topography, the evolution of the periodic surface relief in a pulse-by-pulse fashion may result in ripple curvature of higher order due to laser-induced inhomogeneities.[8,15,17,18,27] A higher order component of the corrugation affects LSPR-RA coupling strength, hence λ_{res} and Q-factor and, ultimately, LSFL formation and periodicity. Moreover, due to the pulse-by-pulse material melting or removal, the ripple depth also increases upon increasing N.[18] To evaluate the impact of the modulation of the surface pattern and depth on the LSFL features in multipulse conditions, rippled topographies of varying order and depth on stainless steel are considered; subsequently, the reflectivity (R) is calculated to investigate the influence of those parameters on λ_{res} and Q-factor. The associated quality factor defined as $Q = \nu_{res}/\Delta\nu$, where ν_{res}

ADVANCED
SCIENCE NEWS

www.advancedsciencenews.com
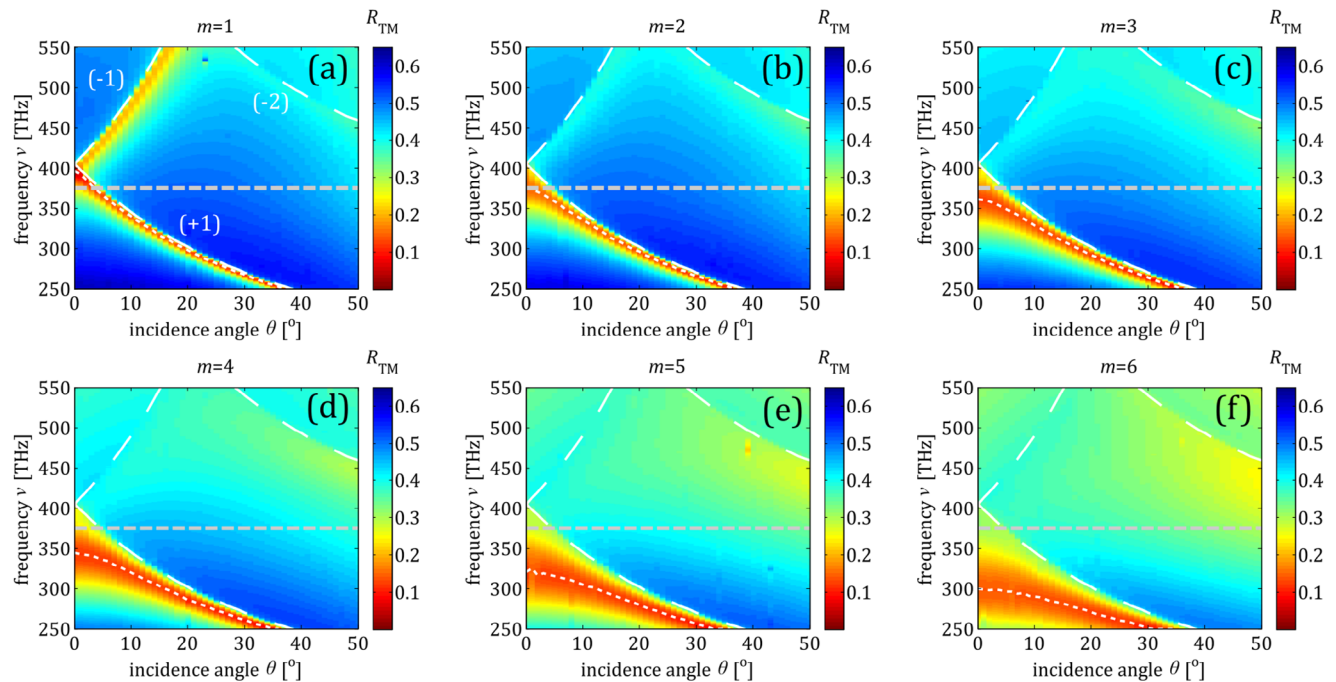
LASER
& PHOTONICS
REVIEWS

www.lpr-journal.org

Figure 4. Angular dispersion characteristics of the hybrid surface modes relative to the laser wavelength. Simulated reflectivity of transverse-magnetic (TM)-polarized light as a function of photon frequency ($\nu = c_0/\lambda$, where c_0 is the speed of light in vacuum) and incidence angle θ from ripples composed of stainless steel with $\alpha = 740$ nm, $d = 100$ nm, and varying ripple order a) $m = 1$, b) $m = 2$, c) $m = 3$, d) $m = 4$, e) $m = 5$, and f) $m = 6$. The horizontal gray dashed line indicates the intended laser frequency for surface structuring, ν_L.

is the spectral dip position and $\Delta\nu$ is the FWHM of the peak obtained from a Lorentzian fit,[31] is calculated in Figure 5.

The following analysis will let us obtain valuable information on the characteristics of the hybrid surface modes, that is dependence on incidence angle (dispersion-flattening), bandwidth-broadening, as well as λ_{res}-shifting, which when examined relative to the laser wavelength (λ_L) are expected to elucidate the requirements for imprinting LSFL ripples of a particular topography. First, we examine the effect of ripple order (m) on λ_{res} and Q-factor (see **Figures 4** and **5**, respectively) by increasing m from 1 to 6. A rippled topography of fixed lattice constant and depth of 740 and 100 nm, respectively, is considered aiming to emu-

late a typical experimentally-attained periodic pattern for a low number of applied pulses ($N < 10$).[15,18,36,37] The results are depicted in Figure 4a–f; the white dashed curves indicate the (−1), (+1), and (+2) RAs in the x–direction (see Equation (3)), the horizontal gray dashed line indicates the intended laser frequency for surface structuring, ν_L, and the white dotted curves are guides for the eye denoting the resonant frequency, ν_{res}, which corresponds to minimum reflection/maximum absorption.

In all cases, the coupling of the LSPRs to the RAs yields the lower SLRs. More specifically, the SLRs are dispersive bands that can deviate considerably from the RAs. The results in Figure 4a–f indicate a clear correlation between the SLR characteristics and
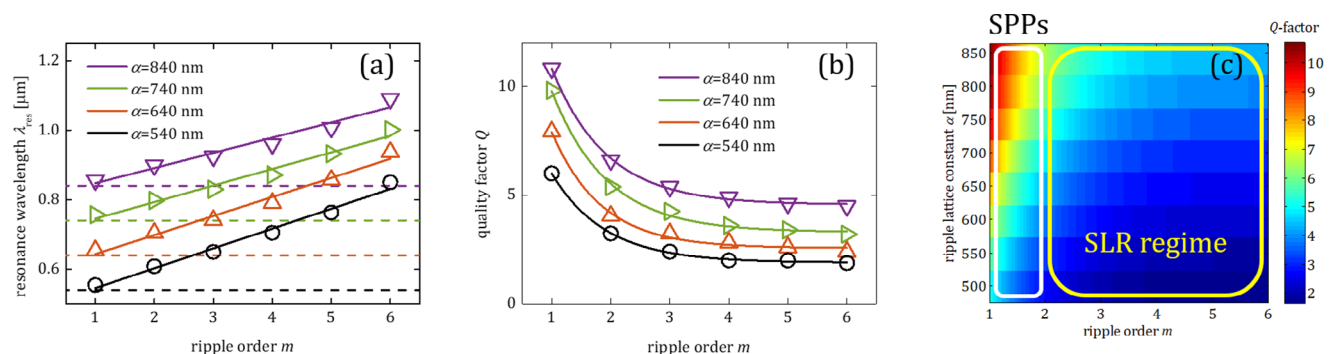

Figure 5. The evolution of a) resonance wavelength (reflection dip/absorption peak) and b) Q-factor as a function of ripple order m, calculated from the simulated reflectivity spectra at normal incidence, for a ripple composed of stainless steel with varying lattice constants of $\alpha = 840$ (purple), 740 (green), 640 (orange), and 540 nm (black). c) Q-factor map plotted as a function of ripple order m and lattice constant α, assuming a fixed depth of $d = 100$ nm. The white and yellow frames in (c) denote the SPP and SLR regimes, respectively.
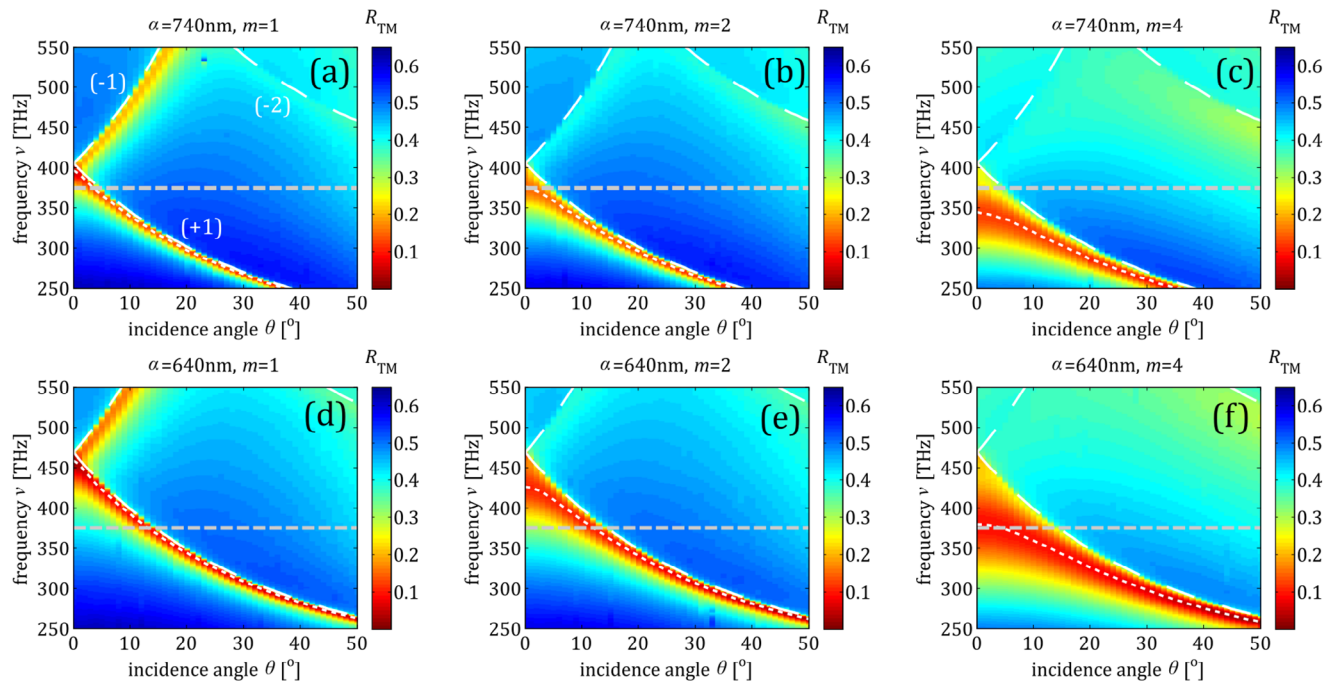
Figure 6. Simulated reflectivity of transverse-magnetic (TM)-polarized light as a function of photon frequency and incidence angle θ from ripples composed of stainless steel with $d = 100$ nm, a,d) $m = 1$, b,e) $m = 2$, c,f) $m = 4$, and a–c) $\alpha = 740$ nm, d–f) $\alpha = 640$ nm. The horizontal gray dashed line indicates the intended laser frequency for surface structuring, ν_L. For lower periodicities, the RA wavelength decreases (see Equation (3) and white dashed curves). Consequently, lower periodicities require higher deviations of λ_{res} from the associated RA for a positive EM feedback process (i.e., to satisfy $\nu_{res} \approx \nu_L$) and therefore higher coupling strengths (broader linewidths) in order to be imprinted.

the order of corrugation due to a change in the coupling strength. As m increases, the SLR shifts toward lower frequencies (deviating more from the RA), but also broadens. As shown in Figure 5, for normal incidence ($\theta = 0$), the increase in coupling strength with increasing m leads to a linear deviation of λ_{res} from the associated RA (Figure 5a) and an exponential decay of the resonance Q-factor (Figure 5b). Moreover, the results in Figure 4 show an angle dependence of λ_{res} and resonance linewidth. As θ increases, the SLR linewidth becomes narrower, and the absorption peak approaches the RA. In contrast, for lower θ, the SLR broadens and deviates in a more pronounced fashion from the RA as it becomes more localized (the dispersion flattens) and resembles an LSPR. These results indicate the hybrid nature of the resonance modes identified in our study examining LIPSS ripples. For instance, Figure 3g,i ($m = 3$) clearly indicates enhanced localized hot spots compared to Figure 3a,c ($m = 1$). This points to localized plasmon resonances. However, for truly localized resonances, which are uncoupled with each other, the angular dispersion is anticipated to be flat. This is not the case in Figure 4, indicating that the localized excitations are coupled across the array. In addition, in the reflectivity spectra (Figures 2 and 4) the corresponding features fall close to the RA, since a propagating/radiation mode is needed to supply the far-field coupling across the array.

The monotonic increase of λ_{res} with m and the broadening of the resonance linewidth due to the increasing coupling strength, as well as the angle dependence of the coupling strength play a critical role in LSFL formation and periodicity. To demonstrate the impact of the monotonic increase of coupling strength on the imprinted ripple periodicity, in **Figure 6a–f**, we plot the re-

flectivity spectra as a function of θ assuming two ripples with different lattice constants of $\alpha = 740$ nm (Figure 6a–c) and $\alpha = 640$ nm (Figure 6d–f), and varying $m = 1, 2, 4$. As seen, for lower (higher) periodicity the RA wavelength decreases (increases) (see Equation (3) and white dashed curves). Consequently, at normal incidence ($\theta = 0$), the condition $\nu_{res} \approx \nu_L$, which would initiate a positive EM feedback process, is satisfied for different m when the periodicity changes, for $m = 2$ when $\alpha = 740$ nm and for $m = 4$ when $\alpha = 640$ nm, respectively (see horizontal gray line versus white dotted curves in Figure 6b,f). Since an increase of m is a proxy for an increase in N (consecutive pulses induce an asymmetry in the ripple profile[15]), the results of Figure 6a–f indicate that LSFL periodicity will decrease with increasing N since it is driven by the aforementioned positive feedback process.

Next, the effect of the ripple depth (d) on the resonance wavelength and resonance linewidth as a function of the incident photon frequency, ν, and the incidence angle, θ, is analyzed (**Figure 7a–c**). Since fluence values near the ablation threshold limit the maximum depth to ≈ 200 nm due to hydrodynamic reasons,[18] Figure 7a–c shows the dispersion information for a ripple with varying depths of 100, 150, and 200 nm, while keeping $m = 2$ and $\alpha = 740$ nm fixed. As in the case where m was varied, when d increases the SLR redshifts but also broadens, demonstrating an enhanced coupling strength. In addition, when d increases the reflectivity minimum becomes deeper. This is due to stronger near fields and higher absorption (see Figure 3i). Consequently, higher depths are expected to boost the coupling strength (see also next section). We note that higher depths (steeper ripples) also provide a smooth transition for the incident wave entering the bulk ma-
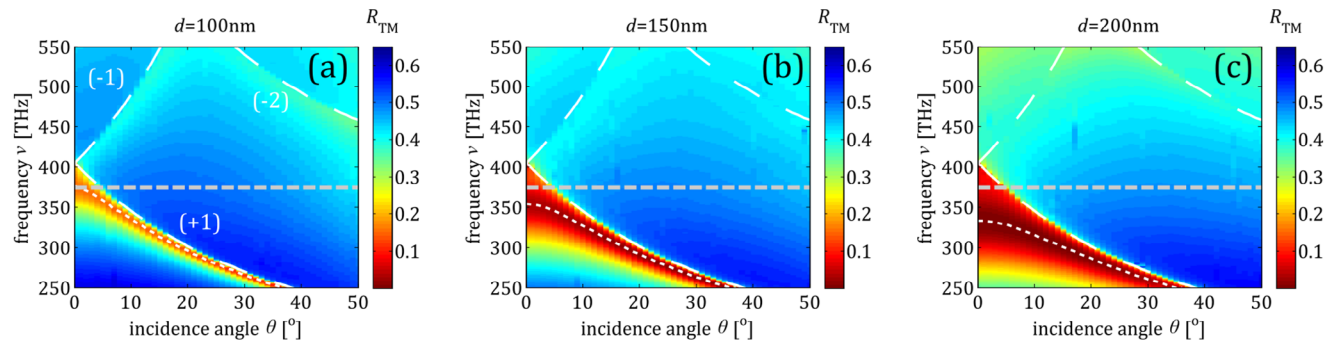
**ADVANCED
SCIENCE NEWS**

www.advancedsciencenews.com

www.lpr-journal.org

LASER
& PHOTONICS
REVIEWS

Figure 7. Simulated reflectivity of transverse-magnetic (TM)-polarized light as a function of photon frequency ($\nu = c_0/\lambda$, where c_0 is the speed of light in vacuum) and incidence angle θ from ripples composed of stainless steel with $\alpha = 740$ nm, $m = 2$, and a) $d = 100$ nm, b) $d = 150$ nm, and c) $d = 200$ nm. The horizontal gray dashed line indicates the intended laser frequency for surface structuring, ν_L.

terial from air, thus reducing reflections due to impedance mismatch and leading to larger absorptivity.

To summarize, the monotonic increase of coupling strength with increasing m and d indicates that a higher order of corrugation and larger depth promotes the formation of LIPSS of smaller periodicities (see also Figure 6a–f). The reason is that lower periodicities require higher deviations of λ_{res} from the associated RA for a positive EM feedback process (i.e., to satisfy $\lambda_{res} \approx \lambda_L$) and therefore higher coupling strengths (broader linewidths). It is noted that while a positive feedback process from pulse to pulse may occur off-resonance too, the transfer of laser fields to the EM mode appears to be less efficient.

2.4. Decrease of LSFL Periodicity and Saturation

In this section, the objective is to elucidate the origin of LSFL periodicity decrease at the increasing number of applied laser pulses (N) as well as the saturation of this phenomenon for high N values.[21,26] A thorough numerical analysis of the ripple formation on stainless steel surfaces is conducted with varying lattice constant, depth, and order of corrugation in the ranges $\alpha = 300$–900 nm, $d = 100$–200 nm, and $m = 1$–7, respectively. This procedure aims to reveal and assess the impact of increasing m and d (or, equivalently, increasing N) on λ_{res} and Q for a broad range of geometry parameters and conditions. In addition, although a broader range of ripple lattice constants (α) is possible to be imprinted (i.e., see broader resonance bandwidth in Figure 6c), the impact of m and d on the dominant LSFL periodicity (Λ) is evaluated assuming that Λ equals the examined ripple's lattice constant ($\Lambda = \alpha$) when the resonance wavelength equals the laser wavelength ($\lambda_{res} \approx \lambda_L$), or, equivalently, when the resonance wavelength shift relative to the laser wavelength equals zero, that is, $\Delta\lambda_{res} = \lambda_{res} - \lambda_L = 0$. It is noted that the above assumptions imply that LIPSS formation results from a positive EM feedback process. The results are shown in **Figure 8a–f**, where we plot $\Delta\lambda_{res}$ as a function of the lattice constant of a ripple with varying m and d. The (+1) RAs along the X–direction (see Equation (3)) are also illustrated for reference (dashed black lines).

The solid curves in Figure 8a ($m = 1$) correspond to the SPP resonant wavelengths and hence the SPP regime (see also Figure 3c). The solid curves in Figure 8b–f ($m \geq 2$) correspond to the SLR resonant wavelengths and hence the SLR regime (see

also Figure 3i). First, for $m = 1$ (Figure 8a), the solid curves are very close to the RA (dashed line). These results indicate that for the conditions considered in this study (see Figure 1), SPPs are not capable of imposing a substantial deviation of λ_{res} from the wavelength of the RA (λ_{RA}) and hence, do not lead to Λ change, that is, for $\Delta\lambda_{res} = 0$ (see horizontal solid line) $\Lambda = \alpha \approx \lambda_{RA}$. As a result, Λ does not decrease substantially, even for ripple depths as large as 600 nm. This result further validates the importance of the coupled SLR surface mode for decreasing LSFL periodicity with N. More specifically, for $m = 2$ (Figure 8b), it appears that there is a shift to self-coupled SLR, a phenomenon that is associated with a high drop in the Q-factor (Figure 5b). According to simulation results illustrated in Figure 8b, the solid curves, corresponding to the SLR case, lie further away from the RA (dashed line), leading to a decrease of Λ, that is, for $\Delta\lambda_{res} = 0$ (see horizontal solid line) $\Lambda = \alpha < \lambda_{RA}$. As m further increases (see Figure 8c), the SLRs deviate more strongly from the associated RA, leading to even smaller values for Λ. Moreover, as d increases (Figure 8d–f), the decrease in Λ becomes even more pronounced (for $m \geq 2$) due to the boosted coupling strength coming from the increased depth (Figure 7).

Besides the Λ decrease with m and d, simulation results (Figure 8) reveal a saturation effect in the evolution of Λ. More specifically, for long lattice constants, λ_{res} redshifts almost linearly with α. On the other hand, for short lattice constants (in conjunction with higher ripple order and depth), λ_{res} stops shifting linearly with α and saturates (see for example $m = 3$ in Figure 8f). This is due to the fact that the LSPRs become quite localized and their coupling along the lattice decreases leading to a flatter geometric dispersion curve. The minimum value for LSFL periodicity is found to be $\Lambda \approx \lambda_L/2 = 400$ nm (see for example $m = 4$ in Figure 8e). The enhanced near-field within the ripple for lower α is further corroborated in Figure 5c, where the Q-factor as a function of α and m is plotted. It is evident that the transition from the SPP to the SLR regime (i.e., from $m = 1$ to $m = 2$) is accompanied by an abrupt decrease in the Q-factor, which decreases even further as α drops. Moreover, the decreasing Q-factor at lower lattice constant values also indicates that the formation of smaller LSFL periodicities is not promoted. Therefore, higher Λ saturation values than $\lambda_L/2$ are expected in typical multipulse experimental studies.[21,26] In summary, simulation results (Figure 8) indicate that Λ can, in principle, reach values as low as $\approx \lambda_L/2$ (see brown, cyan, green, and brown curves in Figure 8c–f,
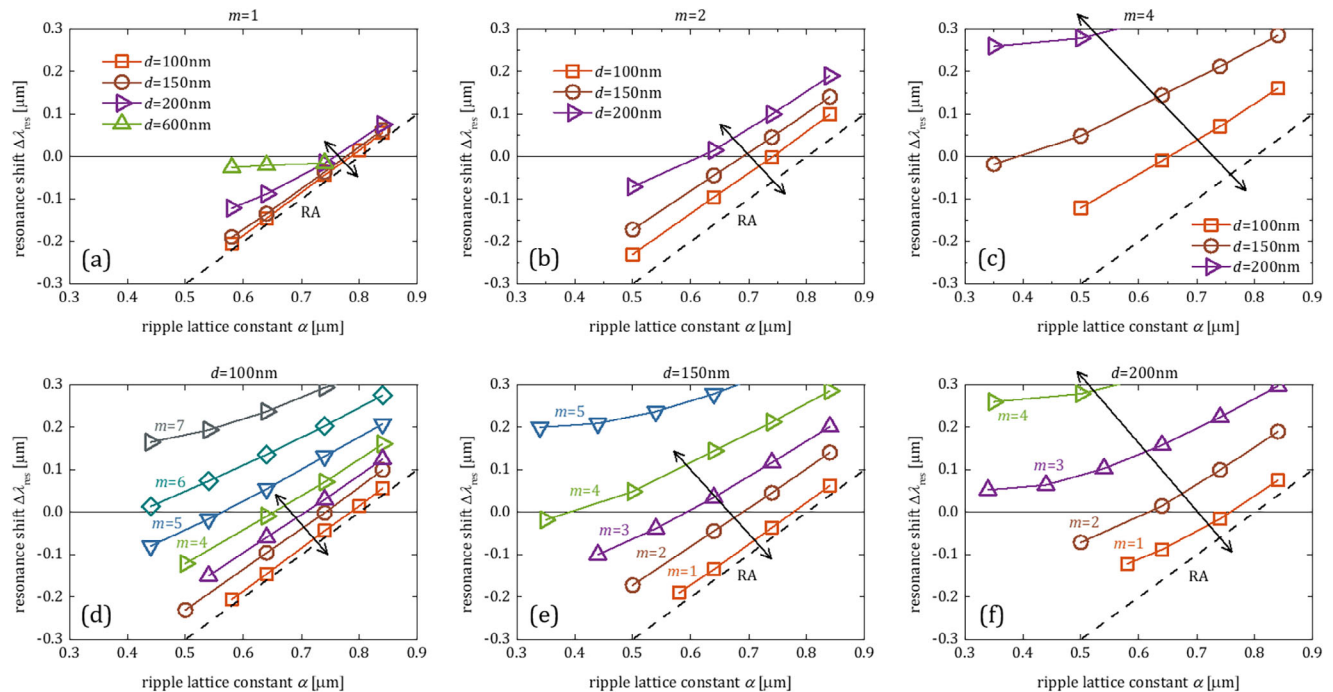
Figure 8. Resonance wavelength shift relative to the laser wavelength ($\lambda_L = 800$ nm), $\Delta\lambda_{res} = \lambda_{res} - \lambda_L$, as a function of ripple's lattice constant, α, for a ripple with varying depths of $d = 100$, 150, 200, and 600 nm and order of corrugation in the range of $m = 1$–7. a) $m = 1$, $d = 100$, 150, 200, and 600 nm, b) $m = 2$, $d = 100$, 150, and 200 nm, c) $m = 4$, $d = 100$, 150, and 200 nm, d) $d = 100$ nm, $m = 1$–7, e) $d = 150$ nm, $m = 1$–5, and f) $d = 200$ nm, $m = 1$–4. The resonance wavelengths are calculated from the simulated reflectivity spectra of the ripples. We also plot the (+1) RA in the x–direction given by Equation (3) (dashed lines), for reference. The horizontal black solid line denotes $\lambda_L \approx \lambda_{res}$, where $\Lambda \approx \alpha$.

respectively). Thus, the theoretical predictions for the periodicities give values in the range $\lambda_L/2$–λ_L, and Λ decreases with increasing m and d (i.e., equivalent to increasing applied laser pulses N[8,15]). Thus, our simulation results predict and verify the previously-only-experimentally-observed lowest limit of LSFL periodicity (i.e., $\lambda_L/2$).[40]

Notably, the results illustrated in Figure 8 agree with experimental studies showing an exponential decay of Λ with N.[21,26] The role of the EM mechanisms in the drop of Λ with N is still debated. In previous reports, a strong correlation of Λ with the ripple depth has been proposed to explain the effect of Λ decrease with N.[8,26] In other works, it was reported that at small N where ripple deepening occurs, Λ remains nearly constant (i.e., Λ does not depend on d); by contrast, Λ decrease occurs at larger N where ripple depth is almost conserved.[15] Our results indicate that the decrease of Λ is dictated by whether the corrugation drives the transition from the SPP to the SLR regime (Figure 8). More specifically, in the SPP regime, Λ is not anticipated to decrease even for depths as high as 600 nm (Figure 8a). Moreover, even if LIPSS depth is conserved, we expect Λ to decrease since the coupling strength increases monotonically with increasing m (Figure 4a–f). The rate of Λ decrease depends on the depth since higher depths result in increased coupling strength (Figure 8d–f). On the other hand, Λ gradually ceases to depend on m or d (see for example $m = 3$ in Figure 8f) due to decoupling of neighboring LSPRs. As a result of this Λ saturation effect, we expect a more rapid Λ decrease at lower m and d, or equivalently at lower N, leading to the characteristic exponential decay of Λ with N. These results are in agreement with the further analysis

presented in the Supporting Information based on experimental input of modulation depths (Figure S5, Supporting Information). An analysis of experimental results following irradiation of 100Cr6 and silicon demonstrates the decrease of the ripple periodicity at an increasing number of pulses in various laser conditions (see Figure S8a,c, Supporting Information). A similar dependency has also been observed in previous works.[1,8,15,21,26,27] As mentioned above, the experimentally observed relation between the ripple periodicity and number of pulses (reported in previous works, also, shown in the Supporting Information) is predicted from the simulations.

2.5. Impact of Material on Hybrid Surface Mode and LSFL Formation

Besides metals, the formation of LSFL structures with an orientation perpendicular to the electric field of the incident beam upon irradiation by fs-laser pulses has also been observed for low-band gap semiconductors (e.g., Si and Ge), whereas in dielectrics the orientation of LSFLs is, typically, parallel to the laser polarization.[14,26] As in the case of metals, the periodicity depends on the pulse number. Moreover, intense laser beams can potentially lead to excitation levels for which a transition of the material to a "metallic" state can be achieved.[14] Particularly for semiconductors, the observation of such topographies has raised a debate regarding the origin of LSFLs on i) whether the propagation of SPPs is essential for the LSFL formation and ii) if materials with a plasmonic-active character is a sine qua non condi-
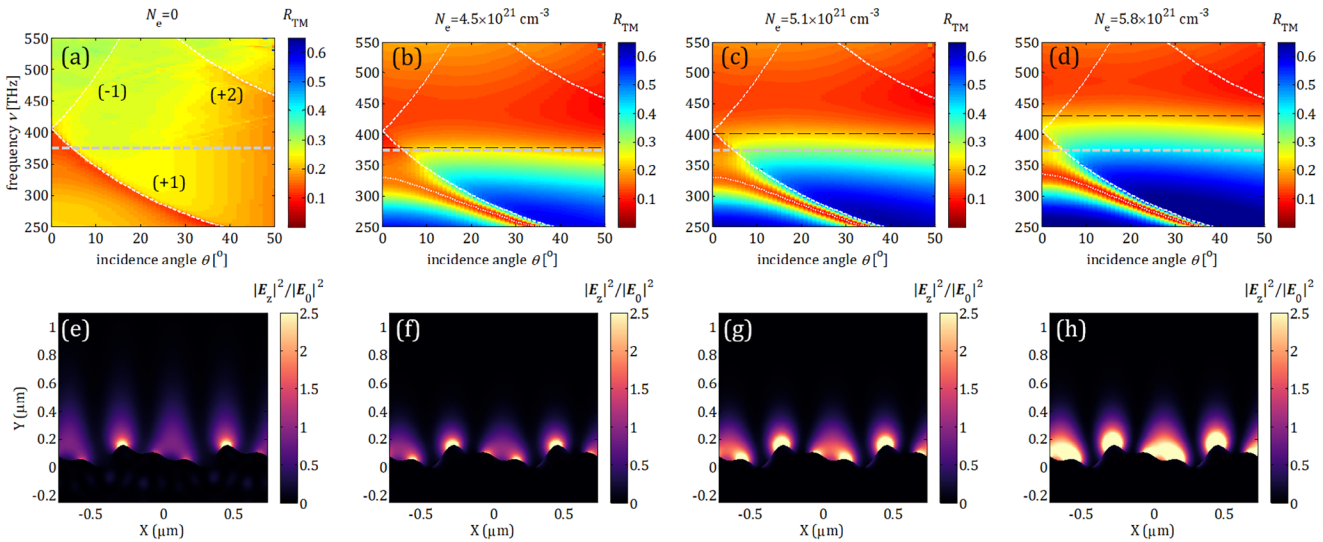
Figure 9. a–d) Simulated reflectivity of transverse-magnetic (TM)-polarized light as a function of photon frequency and incidence angle θ from Si ripples with $\alpha = 740$ nm, $d = 100$ nm, $m = 3$, assuming a) $N_e = 0$, b) $N_e = 4.5 \times 10^{21}$ cm^{-3}, c) $N_e = 5.1 \times 10^{21}$ cm^{-3}, and d) $N_e = 5.8 \times 10^{21}$ cm^{-3}. The horizontal gray dashed line indicates the intended laser frequency for surface structuring, ν_L. The horizontal black dashed line denotes the transition frequency from the dielectric to the plasmonic-inactive and plasmonic regimes. e–h) Normalized electric field intensity of E_z, $|E_z|^2/|E_0|^2$ indicating the SLR surface mode corresponding to e) $N_e = 0$, f) $N_e = 4.5 \times 10^{21}$ cm^{-3}, g) $N_e = 5.1 \times 10^{21}$ cm^{-3}, and h) $N_e = 5.8 \times 10^{21}$ cm^{-3} at the resonance wavelength of 0.773, 0.908, 0.904, and 0.895 µm indicated in panels (a), (b), (c), and (d), respectively (normal incidence).

tion for the generation of these patterns.[8,13,24,41] Given the fact that LSFLs are oriented perpendicularly to the incident polarization, the dominant explanation for LSFLs is that they originate from the excitation and propagation of SPPs, which can only occur when Re(ϵ_m) < −1 (considering an air superstrate). Some other studies report LSFLs on semiconductor surfaces for low excitation levels which do not permit a dielectric to plasmonic transition [e.g., Re(ϵ_m) > −1].[13,24]

To explore the LSFL generation on semiconducting surfaces, the theoretical framework introduced in the previous sections is employed for Si. As in the case of metals, given the pulse number dependence of LSFLs for semiconductors upon irradiation by fs-laser pulses,[21,26] we expect Si ripples to support the excitation of coupled surface modes at higher excitation levels that permit a dielectric to metallic transition. We note that enhanced fields on the interface can, in principle, exist at any interface either dielectric-metal or dielectric-dielectric. For instance, instead of plasmons, Mie-type resonances in all-dielectric or semiconductor configurations could efficiently concentrate EM energy on the material surface and hybridize with the lattice leading to SLRs, which are essentially, Bloch modes due to the coherent scattering by the quasi-periodic index of refraction.[39] On the other hand, to achieve high-Q Mie resonances, both the refractive index contrast and the extinction coefficient are important. Furthermore, in the case of air-dielectric or air-semiconductor interfaces, strong leakage of electromagnetic energy into the non-metallic substrate introduces an additional loss channel, affecting the Q-factor.

To examine the impact of the material on the nature and properties of the surface-scattered EM mode, we consider a Si ripple of fixed lattice constant ($\alpha = 740$ nm), depth ($d = 100$ nm) and order of corrugation ($m = 3$) (i.e., reasonable size for a well-defined ripple pattern on Si)[26] irradiated by an ultrashort laser pulse with $\lambda_L = 800$ nm, a pulse duration of 170 fs, and a fluence of $F = 0.5$

J cm^{-2}. It is noted that these values represent typical excitation conditions for LSFL formation on Si surfaces.[26] The ultrashort laser irradiation of the silicon surface leads to a temporal evolution of the photo-excited carriers with density N_e (see Figure S2e and Equation (S3), Supporting Information), affecting Si refractive index and extinction coefficient (see Figure S2a,b and Equation (S2), Supporting Information).[41–44] More specifically, at the initial stage ($N_e = 0$), the reflectivity spectra of the silicon surface (see Figure S2c, Supporting Information) correspond to typical reflectivity values for the unexcited material ($\epsilon'_{Si} \approx 13.51$). Due to the epsilon-near-zero response of Si at higher N_e (see Figure S2a,e, Supporting Information), the reflectivity spectra exhibit an abrupt transition from low to high reflectivity (see Figure S2c, Supporting Information), leading to three distinct regimes, the dielectric regime ($\epsilon_{Si}' > 0$), the plasmonic-inactive ($−1 < \epsilon_{Si}' < 0$), and the plasmonic regime ($\epsilon_{Si}' \leq −1$). In our study, we analyze four different stages of N_e evolution (see Figure S2a,b,e, Supporting Information) corresponding to unexcited Si, where $N_e = 0$ ($\epsilon_{Si} = 13.51 + 0.04i$ for $\lambda = 800$ nm), excited non-plasmonic for $\lambda = 800$ nm (not supporting SPP propagation), where $N_e = 4.5 \times 10^{21}$ m^{-3} ($\epsilon_{Si} = −0.24 + 4.9i$ for $\lambda = 800$ nm), and plasmonic Si for $\lambda = 800$ nm (supporting collective charge oscillations) for an intermediate $N_e = 5.1 \times 10^{21}$ m^{-3} ($\epsilon_{Si} = −1.92 + 5.49i$ for $\lambda = 800$ nm) and the highest $N_e = 5.8 \times 10^{21}$ m^{-3} ($\epsilon_{Si} = −4.2 + 6.3i$ for $\lambda = 800$ nm). The results are summarized in **Figure 9a–h**.

In the initial stage ($N_e = 0$), weak electric field hot spots are observed on the Si surface (Figure 9e), resulting from diffractive coupling.[45] Since Si is dielectric (unexcited), the electromagnetic energy is further transmitted into the non-metallic substrate, which does not favor the EM field confinement on the air-Si interface (hence LSFL formation), resulting in the broadband spectrum and low Q-factor. This is further corroborated in Figure 9e, where we observe the characteristic spatial field distri-

bution of SLR, albeit without pronounced field enhancement. On the other hand, these results suggest that the formation of LSFL perpendicular to the laser polarization seems possible even for non-excited semiconductors but inefficient for typical laser processing configurations (Figure 1), unless using more complex structures aimed to confine light along the propagation direction. This could be achieved by the index contrast in thin films for example.[34]

By contrast, at a higher laser energy dose ($N_e \geq 4.5 \times 10^{21}$ cm^{-3} – Figure 9b–d), we observe a distinct resonance within the plasmonic spectral regime whose dispersion and linewidth are mainly dictated by intrinsic material loss. In Figure 9f–h, we observe the characteristic spatial field distribution of SLRs. The SLR associated with plasmonic-inactive and plasmonic-active regimes exhibits an enhanced EM field (see Figure 9e versus 9f–h), similar to metals (Figure 3i). Consequently, the plasmonic SLR becomes sharper with increasing N_e (i.e., with enhanced Q-factor) since the material becomes more "metallic" leading to a sharper SLR resonance (Figure 9f–h). The above results indicate that SLRs can exist even in unexcited or plasmonic-inactive semiconductors for typical ripple dimensions (Figure 9e) in agreement with several studies reporting LSFL on plasmonic-inactive semiconductors.[13,24] However, plasmonic SLRs exhibit stronger field enhancement (higher Q-factors) that further increases at higher carrier densities (see Figure 9f–h). Therefore, we conclude that plasmonic-active material (supporting collective charge oscillations or SPP propagation) is not fundamentally necessary for LSFL formation perpendicular to the polarization. However, we expect materials with a plasmonic-active optical property to enhance LSFL formation. For instance, several experimental studies report LSFL formation at higher fluences associated with higher N_e (see Equation (S3), Supporting Information).[26] Other studies report that the resulting LSFL periodicity corresponds to the highest N_e experienced along the temporal evolution of photo-excited carriers during the pulse.[46] Finally, the excitation of plasmonic-type SLRs on semiconductors, depending on the generated carrier density and thus laser fluence (see Figure 9f–h), suggests that they could exhibit pulse number dependence upon irradiation by fs-laser pulses analogously to metals (as shown in the previous section). This has been reported in experimental studies[21,26] as well, validating our analysis.

Figure 9b–d also reveals an insignificant influence of N_e on the resonance shift (relative to λ_{RA}—see white dashed curves for $\theta = 0$), and therefore on the coupling strength, for typical laser fluences and hence N_e values (see Figure S2e and Equation (S3), Supporting Information). Consequently, a negligible impact of the laser fluence and N_e on the ripple periodicity is expected. An analysis of experimental results following irradiation of 100Cr6 and silicon demonstrates that the ripple periodicity is not affected by the laser fluence for moderately high and larger values of the fluence (see Figure S8b,d, Supporting Information). A similar dependency has also been revealed in previous reports.[1,8,21,47] Nevertheless, some further investigation is possibly required to elucidate the underlying mechanism that accounts for a very slight rise with fluence of the ripple periodicity (see refs. [1, 8, 21, 47] and Supporting Information).

We note that a surface-scattered field with a direction perpendicular to the incident polarization is a general property of plasmonic surfaces.[48] On unexcited semiconductor or dielectric surfaces, the scattered field by initial nano-roughness is oriented parallel to the incident polarization.[48] Moreover, for SLR excitation, the radiative neighboring coupling should be along the X–axis between adjacent ridges (Figure 1), thus, parallel to the polarization of the incident field (Figure 3h). Therefore, LSFL initiation and growth on unexcited semiconductors require forming patterns oriented perpendicular to the incident polarization or appearing together with LIPSS patterns of different electromagnetic origins and perpendicular orientation to the laser polarization, acting as the precursor. Interestingly, several studies report the successive or simultaneous initiation and growth of LSFL on unexcited Si after regular (or irregular) high spatial-frequency LIPSS patterns of lower periodicity and different EM origins (widely known as HSFL type-r) are formed perpendicular to the laser polarization.[13,24]

A challenging question arising from the above discussion on the various electromagnetic modes excited from the corrugation on the material during repetitive irradiation and localization of energy at specific points on the surface or inside the material could also provide sufficient insight into eminent phenomena such as incubation effects. These phenomena have been observed in various materials (i.e., metals,[49] semiconductors,[50] polymers,[51] and insulators[52]). As a result, significantly lower damage of the irradiated material at pulse energies far below the single-shot ablation threshold following repetitive irradiation occurs. The origin of incubation is still debated; however, it is generally attributed to laser-induced defects or irregularities. To relate the discussion presented in this study with the emergence of regions in/on the material that can facilitate the generation of incubation phenomena, one could argue that processes that can be intrinsic and characteristic (for each category of materials) could lead to the formation of defects that can induce the excitation of electromagnetic modes similar to those investigated in this study. Thus, a rigorous exploration of the features of these modes can provide a more precise evaluation of the magnitude of the absorbed energy from the material which is important to determine the damage conditions, correlate the pulse-by-pulse irradiation impact with the defect generation, and improve our understanding on the origin of incubation. Although such an investigation is beyond the scope of the current work, it is emphasized that our approach could set the basis for the exploration of the underlying physical process of incubation effects.

Finally, it will be interesting to elaborate on whether the methodology in this work can also interpret electromagnetic phenomena and processes that account for the formation of other types of structures that are observed at higher excitation levels. More specifically, a theoretical model (supported by experimental observations[21,28,53]) predicted the formation of supra-wavelength structures (termed as grooves) and protrusions (coined as spikes[28,53] or cone-line protrusions[54]); in those studies, it was proposed that the surface plasmon excitation is suppressed due to the enhanced roughness at high excitation levels and, therefore, other mechanisms (based on the development of hydrothermal waves) are responsible for the fabrication of those structures. This, for instance, can be further supported by the results illustrated in Figure 8c–f and/or in Figure 7b,c. It is shown that an increase in the order of corrugation m leads to a flatter geometric dispersion curve (e.g., see $m = 3$ in Figure 8f), which does not promote LSFL formation associated with the periodic

SPP or SLR with size of the order of the laser wavelength (see decreasing Q-factor as m increases in Figure 5b). Moreover, an enhanced energy deposition on the surface due to impedance matching at higher depths (Figure 7b,c) is expected to suppress after a point the periodic intensity variation deposited on the surface associated with the surface wave (e.g., see broader resonance bandwidth in Figure 7b–d denoting lower Q-factors). These findings indicate, first, that the groove formation mechanism is of a different origin than the LSFL (see SEM images in Figure S9, Supporting Information); on the other hand, the simulation results indicate that the laser conditions (such as fluence and number of pulses) and relevant excitation levels are possible to set the basis for an understanding of the transition from one type of topography to another.

Our investigation, in the present section, demonstrated that irrespective of the material property, the electromagnetic origin of LSFL can be attributed to the frequency-detuning between a localized mode (plasmonic or Mie-type depending on the material) and a propagating/radiation mode (grazing higher diffraction order in our case) due to their coupling/hybridization. The detailed analysis in the present Article revealed the impact of ripple depth, inhomogeneity, and material on the coupling strength, electric field spatial distribution, and associated near-field scattering, and, hence, on LSFL formation and periodicity. The conclusions extracted on the nature and properties of the hybrid modes may also be used as a guide for different configurations (e.g., thin films). Indicatively, the magnitude of the interaction between propagating and localized modes naturally affects LSFL formation/suppression and properties (periodicity, saturation, etc.), since it is associated with the resonance Q-factor and frequency detuning. For instance, as in the case where a Rayleigh anomaly (RA) provides far-field coupling between the individual localized resonances, the same coupling effect may emerge from a guided mode of a slab waveguide. Therefore, the presented methodology constitutes a universal electromagnetic analysis and a guide that can be employed to interpret the LSFL manifestation irrespective of the irradiated material and configuration.

3. Conclusions

We have demonstrated a novel approach for elucidating the induced electromagnetic processes related to LIPSS formation and periodicity tuning which are not material- or geometry-specific. A detailed numerical analysis for a broad range of frequencies and incident angles revealed the origin, properties, and interplay of the excited electromagnetic surface modes as a function of varying ripple depth, inhomogeneity (Fourier components), and material, emulating realistic multipulse conditions. The thorough investigation showed two distinct regimes responsible for determining LIPSS formation and periodicity: the first regime is associated with an electromagnetic field of high intensity generating LSFL formation, while the second regime is related to the excitation of an enhanced near-field that accounts for the LSFL periodicity decrease. Simulation results predict and verify the previously-only-experimentally-observed lowest limit of LSFL periodicity (i.e., $\lambda_L/2$) and derive a practically unaffected ripple periodicity from the laser fluence. We have also shown that plasmonic-active materials are not fundamentally necessary for LSFL formation perpendicular to the polarization. Theoretical

predictions for the induced LIPSS features and their correlation with the laser parameters presented in this study are expected to promote physical understanding and aid in the generation of desired topographies for a plethora of applications.

Supporting Information

Supporting Information is available from the Wiley Online Library or from the author.

Conflict of Interest

The authors declare no conflict of interest.

Data Availability Statement

The data that support the findings of this study are available from the corresponding author upon reasonable request.

[1] E. Stratakis, J. Bonse, J. Heitz, J. Siegel, G. D. Tsibidis, E. Skoulas, A. Papadopoulos, A. Mimidis, A. C. Joel, P. Comanns, J. Krüger, C. Florian, Y. Fuentes-Edfuf, J. Solis, W. Baumgartner, *Mater. Sci. Eng., R* **2020**, *141*, 100562.

[2] A. Papadopoulos, E. Skoulas, A. Mimidis, G. Perrakis, G. Kenanakis, G. D. Tsibidis, E. Stratakis, *Adv. Mater.* **2019**, *31*, 1901123.

[3] G. Perrakis, A. C. Tasolamprou, G. Kenanakis, E. N. Economou, S. Tzortzakis, M. Kafesaki, *Sci. Reports* **2021**, *11*, 11552.

[4] D. Yuan, J. Huang, J. Li, W. Cai, H. Han, Y. J. Liu, M. Wang, S. Xu, D. Yuan, J. Huang, J. Li, H. Han, S. Xu, W. Cai, Y. J. Liu, M. Wang, *Adv. Opt. Mater.* **2023**, *11*, 2202585.

[5] A. C. Tasolamprou, E. Skoulas, G. Perrakis, M. Vlahou, Z. Viskadourakis, E. N. Economou, M. Kafesaki, G. Kenanakis, E. Stratakis, *Sci. Reports* **2022**, *12*, 19769.

[6] E. Babaliari, P. Kavatzikidou, D. Angelaki, L. Chaniotaki, A. Manousaki, A. Siakouli-Galanopoulou, A. Ranella, E. Stratakis, *Int. J. Mol. Sci.* **2018**, *19*, 2053.

[7] A. Francone, S. Merino, A. Retolaza, J. Ramiro, S. A. Alves, J. V. de Castro, N. M. Neves, A. Arana, J. M. Marimon, C. M. S. Torres, N. Kehagias, *Surf. Interfaces* **2021**, *27*, 101494.

[8] M. Huang, F. Zhao, Y. Cheng, N. Xu, Z. Xu, *ACS Nano* **2009**, *3*, 4062.

[9] H. M. Van Driel, J. E. Sipe, J. F. Young, *Phys. Rev. Lett.* **1982**, *49*, 1955.

ADVANCED
SCIENCE NEWS

www.advancedsciencenews.com

LASER
& PHOTONICS
REVIEWS

www.lpr-journal.org

[10] J. E. Sipe, J. F. Young, J. S. Preston, H. M. Van Driel, *Phys. Rev. B* **1983**, *27*, 1141.

[11] D. A. Ketzaki, O. Tsilipakos, T. V. Yioultsis, E. E. Kriezis, *J. Appl. Phys.* **2013**, *114*, 113107.

[12] J. Geng, W. Yan, L. Shi, M. Qiu, *Nano Lett.* **2022**, *22*, 9658.

[13] J. Z. P. Skolski, G. R. B. E. Römer, J. Vincenc Obona, A. J. Huis In 'T Veld, *J. Appl. Phys.* **2014**, *115*, 103102.

[14] A. Rudenko, J. P. Colombier, S. Höhm, A. Rosenfeld, J. Krüger, J. Bonse, T. E. Itina, *Sci. Rep.* **2017**, *7*, 12306.

[15] A. Rudenko, C. Mauclair, F. Garrelie, R. Stoian, J. P. Colombier, *Nanophotonics* **2019**, *8*, 459.

[16] F. Fraggelakis, G. Mincuzzi, I. Manek-Hönninger, J. Lopez, R. Kling, *RSC Adv.* **2018**, *8*, 16082.

[17] A. Borowiec, M. Couillard, G. A. Botton, H. K. Haugen, *Appl. Phys. A: Mater. Sci. Process.* **2004**, *79*, 1887.

[18] A. Rudenko, C. Mauclair, F. Garrelie, R. Stoian, J. P. Colombier, *Phys. Rev. B* **2019**, *99*, 235412.

[19] J. Bonse, M. Munz, H. Sturm, *J. Appl. Phys.* **2004**, *97*, 013538.

[20] H. Zhang, J. P. Colombier, S. Witte, *Phys. Rev. B* **2020**, *101*, 245430.

[21] G. D. Tsibidis, A. Mimidis, E. Skoulas, S. V. Kirner, J. Krüger, J. Bonse, E. Stratakis, *Appl. Phys. A: Mater. Sci. Process.* **2018**, *124*, 27.

[22] A. Ajami, A. A. Ionin, S. I. Kudryashov, S. V. Makarov, T. Ganz, A. Assion, C. S. R. Nathala, W. Husinsky, *Opt. Express* **2015**, *23*, 5915.

[23] J. Bonse, S. Höhm, A. Rosenfeld, J. Krüger, *Appl. Phys. A: Mater. Sci. Process.* **2013**, *110*, 547.

[24] H. Zhang, J. P. Colombier, C. Li, N. Faure, G. Cheng, R. Stoian, *Phys. Rev. B: Condens. Matter Mater. Phys.* **2015**, *92*, 174109.

[25] J. Bonse, S. Gräf, *Nanomater* **2021**, *11*, 3326.

[26] J. Bonse, J. Krüger, *J. Appl. Phys.* **2010**, *108*, 034903.

[27] A. Abou Saleh, A. Rudenko, L. Douillard, F. Pigeon, F. Garrelie, J. P. Colombier, *ACS Photonics* **2019**, *6*, 2287.

[28] G. D. Tsibidis, C. Fotakis, E. Stratakis, *Phys. Rev. B: Condens. Matter Mater. Phys.* **2015**, *92*, 041405.

[29] A. Rudenko, A. Abou-Saleh, F. Pigeon, C. Mauclair, F. Garrelie, R. Stoian, J. P. Colombier, *Acta Mater.* **2020**, *194*, 93.

[30] W. Barnes, T. Preist, S. Kitson, J. Sambles, *Phys. Rev. B: Condens. Matter Mater. Phys.* **1996**, *54*, 6227.

[31] T. Christopoulos, O. Tsilipakos, O. Tsilipakos, G. Sinatkas, E. E. Kriezis, *Opt. Express* **2019**, *27*, 14505.

[32] P. Lingos, G. Perrakis, O. Tsilipakos, G. D. Tsibidis, E. Stratakis, *Opt. Laser Technol.* **2023**, *163*, 109415.

[33] G. Perrakis, O. Tsilipakos, G. Kenanakis, M. Kafesaki, C. M. Soukoulis, E. N. Economou, *Opt. Express* **2019**, *27*, 6842.

[34] Z. Zhang, P. Liu, W. Lu, P. Bai, B. Zhang, Z. Chen, S. A. Maier, J. Gómez Rivas, S. Wang, X. Li, *Fundam. Res.* **2022**, *3*, 822.

[35] P. B. Johnson, R. W. Christy, *Phys. Rev. B* **1974**, *9*, 5056.

[36] J. Bonse, R. Koter, M. Hartelt, D. Spaltmann, S. Pentzien, S. Höhm, A. Rosenfeld, J. Krüger, *Appl. Phys. A: Mater. Sci. Process.* **2014**, *117*, 103.

[37] P. Gregorčič, M. Sedlaček, B. Podgornik, J. Reif, *Appl. Surf. Sci.* **2016**, *387*, 698.

[38] V. G. Kravets, A. V. Kabashin, W. L. Barnes, A. N. Grigorenko, *Chem. Rev.* **2018**, *118*, 5912.

[39] A. Abass, S. R. K. Rodriguez, J. Gómez Rivas, B. Maes, *ACS Photonics* **2014**, *1*, 61.

[40] J. Bonse, S. Hohm, S. V. Kirner, A. Rosenfeld, J. Kruger, *IEEE J. Sel. Top. Quantum Electron.* **2017**, *23*, 109.

[41] J. P. Colombier, A. Rudenko, E. Silaeva, H. Zhang, X. Sedao, E. Bévillon, S. Reynaud, C. Maurice, F. Pigeon, F. Garrelie, R. Stoian, *Phys. Rev. Res.* **2020**, *2*, 043080.

[42] G. D. Tsibidis, M. Barberoglou, P. A. Loukakos, E. Stratakis, C. Fotakis, *Phys. Rev. B: Condens. Matter Mater. Phys.* **2012**, *86*, 115316.

[43] E. D. Palik, *Handbook of Optical Constants of Solids*, Vol. *II*, Academic Press, Cambridge, MA **1998**.

[44] K. Sokolowski-Tinten, D. von der Linde, *Phys. Rev. B* **2000**, *61*, 2643.

[45] B. Auguié, W. L. Barnes, *Phys. Rev. Lett.* **2008**, *101*, 143902.

[46] K. Cheng, J. Liu, K. Cao, L. Chen, Y. Zhang, Q. Jiang, D. Feng, S. Zhang, Z. Sun, T. Jia, *Phys. Rev. B* **2018**, *98*, 184106.

[47] K. Okamuro, M. Hashida, Y. Miyasaka, Y. Ikuta, S. Tokita, S. Sakabe, *Phys. Rev. B: Condens. Matter Mater. Phys.* **2010**, *82*, 165417.

[48] A. Rudenko, C. Mauclair, F. Garrelie, R. Stoian, J. P. Colombier, *Appl. Surf. Sci.* **2019**, *470*, 228.

[49] J. Güdde, J. Hohlfeld, J. G. Müller, E. Matthias, *Appl. Surf. Sci.* **1998**, *127–129*, 40.

[50] J. Bonse, J. M. Wrobel, J. Krüger, W. Kautek, *Appl. Phys. A: Mater. Sci. Process.* **2001**, *72*, 89.

[51] S. Küper, M. Stuke, *Appl. Phys. A: Solids Surf.* **1989**, *49*, 211.

[52] A. Rosenfeld, M. Lorenz, R. Stoian, D. Ashkenasi, *Appl. Phys. A: Mater. Sci. Process.* **1999**, *69*, S373.

[53] E. Allahyari, J. J. J. Nivas, E. Skoulas, R. Bruzzese, G. D. Tsibidis, E. Stratakis, S. Amoruso, *Appl. Surf. Sci.* **2020**, *528*, 146607.

[54] V. Villerius, H. Kooiker, J. Post, Y. T. Pei, *Int. J. Mach. Tools Manuf.* **2019**, *138*, 27.